Pressure-induced transition in the multiferroic CoCr_{2}O_{4} spinel

I. Efthimiopoulos, Z. T. Y. Liu, S. V. Khare, P. Sarin, T. Lochbiler, V. Tsurkan, A. Loidl, D. Popov, and Y. Wang

Phys. Rev. B **92**, 064108 — Published 12 August 2015

DOI: 10.1103/PhysRevB.92.064108

Pressure-induced transition in the multiferroic $CoCr_2O_4$ spinel

I. Efthimiopoulos[1*], Z. T. Y. Liu[2], S. V. Khare[2], P. Sarin[3], T. Lochbiler[1], V. Tsurkan[4,5], A. Loidl[4], D. Popov[6], and Y. Wang[1*]

[1]*Department of Physics, Oakland University, Rochester, MI 48309, USA*

[2]*Department of Physics, University of Toledo, Toledo, OH 43606, USA*

[3]*School of Materials Science and Engineering, Oklahoma State University, Tulsa,OK 74106, USA*

[4]*Experimental Physics 5, Center for Electronic Correlations and Magnetism, Institute of Physics, University of Augsburg, D-86159 Augsburg, Germany*

[5]*Institute of Applied Physics, Academy of Sciences of Moldova, MD 2028 Chisinau, Republic of Moldova*

[6]*High Pressure Collaborative Access Team, Geophysical Laboratory, Carnegie Institution of Washington, Argonne, IL 60439, USA*

We have explored the high-pressure structural, vibrational, electronic, and magnetic behavior of the multiferroic $CoCr_2O_4$ spinel up to 30 GPa by means of x-ray diffraction, Raman spectroscopy, and density functional theory calculations. Our investigations revealed a reversible tetragonal distortion of the starting cubic structure above 16 GPa. We suggest that the structural modification is mainly driven by magnetic effects induced under pressure. The obtained results are compared with the high-pressure behavior of related spinels.

PACS numbers: 61.50.Ks, 75.50.Gg, 71.20.-b

I. INTRODUCTION

The family of $ACr^{3+}{}_2X_4$ spinels (A^{2+}=Mn-Zn, Cd, Hg; X^{2-}=O, S, Se) has recently reattracted significant attention, owing to the discovery of multiferroic properties in several of its members[1–4]. These compounds have been studied extensively over the years due to the intimate coupling between their structural, electronic, and magnetic properties[5–7]. For example, significant magnetoelastic coupling takes place near the magnetic ordering temperatures for these systems, accompanied frequently by structural transitions[6–8]. More recent investigations indicate the close connection between the structure and macroscopic electrical polarization for the multiferroic Cr-based spinels[4,9,10].

Given this strong interrelation between structural, vibrational, magnetic, and electronic degrees of freedom, the variation of lattice by external pressure provides an appealing method for tuning the physical properties of these materials. Actually, several high-pressure studies reveal structural[11–13], electronic[13,14], and magnetic[13,15] transitions/changes for Cr-based spinels upon compression.

Here we focus on the effect of pressure on the structure, lattice dynamics, and magnetism of the multiferroic $CoCr_2O_4$. At ambient conditions, $CoCr_2O_4$ crystallizes in the normal spinel structure (SG *Fd*-3*m*, *Z*=8, **Fig. 1**) In this phase, the orbitally-inactive Co^{2+} ($3d^7$: e^4 $t_2{}^3$) and Cr^{3+} ($3d^3$: $t_{2g}{}^3$ $e_g{}^0$) cations occupy tetrahedral and octahedral sites, respectively. Upon lowering temperature, $CoCr_2O_4$ undergoes three successive magnetic transitions[16,17] due to the competing Cr-Cr, Co-Cr, and Co-Co exchange interactions: ferrimagnetic ordering sets in below T_C≈95 K, followed by a transition into an incommensurate conical-spiral state at T_S≈26 K. Lowering temperature further leads to an incommensurate-to-commensurate transition at T_L≈14 K. In addition, spin-induced ferroelectricity has been observed below T_S[3,18,19], thus making $CoCr_2O_4$ multiferroic; more recent studies, however, place the coupling between magnetic moments and electric dipoles below T_C already[20,21]. Quite interestingly, $CoCr_2O_4$ retains its starting cubic symmetry down to 10 K[7,22], even though a structural modification has been speculated below T_C[21].

The available high-pressure investigations on this material have focused on the dependence of the various magnetic ordering temperatures[23–25]. From these studies, it is shown that pressure enhances all of the T_C, T_L, and T_S in almost similar rates. Since structural data are lacking, however, the microscopic picture for understanding this pressure-induced increase of the magnetic frustration remains incomplete. Here, we report on the effect of pressure on the structural and vibrational properties of $CoCr_2O_4$ up to 30 GPa by means of x-ray diffraction (XRD) and Raman spectroscopy, respectively. Our experimental results are complemented by density functional theory (DFT) calculations of the electronic and magnetic properties of $CoCr_2O_4$ under compression.

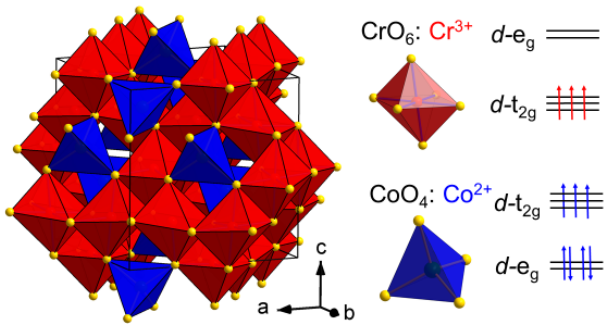

FIG. 1: (Color online) Polyhedral view of the crystal structure of $CoCr_2O_4$ spinel at ambient conditions (SG *Fd*-3*m*, *Z*=8). The blue and red polyhedra represent the CoO_4 tetrahedra and the edge-sharing CrO_6 octahedra.

II. EXPERIMENTAL AND COMPUTATIONAL DETAILS

Details of the sample synthesis have been reported elsewhere[16]. Pressure was generated with a symmetric diamond anvil cell (DAC), equipped with 300 μm culet diamonds. The ruby luminescence method was employed for pressure calibration[26].

The monochromatic angle-dispersive high-pressure XRD measurements were performed at the 16BM-D beamline of the High Pressure Collaborative Access Team, at the Advanved Photon Source of Argonne National Laboratory. The x-ray beam wavelength was λ=0.4246 Å. The measured XRD diffractograms were processed with the FIT2D software[27]. Refinements were performed using the GSAS+EXPGUI software packages[28,29]. The *P-V* data were fitted with a Birch-Murnaghan equation of state[30] (B-M EOS). Helium served as a pressure transmitting medium (PTM).

The high-pressure Raman spectroscopic studies were conducted on single-crystalline $CoCr_2O_4$ samples with a solid-state laser (λ = 532 nm) coupled to a single-stage Raman spectrometer (Andor S500i) and a charge-coupled device. The size of the laser spot on the sample surface was approximately 30 μm, whereas the laser power was 3 mW measured outside the DAC. Both helium and a mixture of methanol-ethanol-water 16:3:1 served as PTM in separate runs.

The *ab initio* density functional theory (DFT) calculations have been performed with the Vienna *Ab initio* Simulation Package[31–34]. Potentials of Co, Cr_pv, and O using projector-augmented wave method[35,36] were selected, with PBE generalized gradient approximation (GGA)[37,38]. Because transition metal oxides are correlated materials, GGA+U correction scheme was used for the *d* orbitals of Co and Cr. The *U* values were chosen to be 3.3 for Co and 3.7 for Cr[39,40]. The plane wave cutoff energy was chosen to be 520 eV to ensure lattice parameter relaxations. During the electronic iterations, Gaussian smearing was used with a sigma value as small as 0.1 eV, until the convergence criterion of 10^{-5} eV was reached. During each run, the atomic positions (internal parameters) were allowed to freely relax according to the cell symmetry.

Care was taken to construct the cells with various magnetic configurations. We used the special quasi-random structure generation algorithm[41,42] provided in the

Alloy Theoretic Automated Toolkit[43,44] to obtain the paramagnetic cubic spinel structure, with a binary spin-up and spin-down construction for the Co^{2+} and Cr^{3+} to maintain 0 total magnetic moments for each species, respectively. The Γ-centered k-point, 2 × 2 × 2, mesh was selected. For the ferrimagnetic tetragonal structure, all Co^{2+} were given spin-up states, and half of Cr^{3+} in the same plane on the *c*-axis were given spin-up states, the other half spin-down, simulating the experimental configuration[17]. The Γ-centered k-point, 3 × 3 × 3, mesh was selected. The *c*-axis was allowed to freely relax against *a* and *b* for each manually set volume. In both magnetic constructions, each magnetic moment was set to be 3 μ_B in magnitude, and their values stayed around 2.7 μ_B (Co^{2+}) and 2.9 μ_B (Cr^{3+}) throughout the electronic iterations without sign change.

To obtain the equilibrium lattice constants, we picked 6 volume values covering the equilibrium volume and fit the total energy to a B-M EOS[30]. We then obtained the pressure values of each volume from the $P(V)$ formulation of the same EOS. The total density of states (TDOS) were calculated with k-points meshes of twice the division number than stated above. Bader charge transfer analysis[45–47] was done with the implementation following the theoretical guidelines[48,49], as described elsewhere[50–53]. The fast Fourier transform grid for charges was set at 300 × 300 × 300.

III. RESULTS AND DISCUSSION

A. Structural properties under pressure

The $CoCr_2O_4$ compound retains the cubic spinel structure up to 16 GPa (**Fig. 2**); both the lattice and interatomic parameters of the *Fd*-3*m* phase could be obtained up to that pressure (**Figs. 3&4**). Further compression leads to a *reversible*[54] asymmetric broadening for specific Bragg peaks [**Fig.2(b)**]. Possible reasons behind this Bragg peak broadening might be non-hydrostatic conditions, cationic inversion, or a structural transition. Since we have employed helium as a PTM in our XRD experiment, we can most likely exclude any non-hydrostatic effects as the cause behind this effect.

As for the possibility of a pressure-induced (partial) cationic inversion, i.e. the mutual cationic exchange in the tetrahedral and octahedral spinel sites, it is quite frequent for spinels under pressure[55,56]. In order to check this inversion scenario, we have compared the ambient-pressure cubic lattice parameter *a* and that of the fully decompressed sample[54]; such direct comparison can provide insight on any structural damage or disorder suffered by the material upon compression[56,57]. Since the *a* of the starting and the decompressed samples are very close, we can safely exclude any *permament* disorder taking place in $CoCr_2O_4$. On the other hand, a more local probe such as Raman spectroscopy is more suitable for identifying microstructural changes. Actually, the partial inversion of the spinel structure would result in the appearance of sidebands in the high-frequency stretching modes due to the different cationic sizes[58]. Since we could not detect such "new" modes in the Raman spectra of $CoCr_2O_4$ near the transition pressure (**Fig. 5**), we exclude the possibility of a pressure-induced

cationic inversion in $CoCr_2O_4$. Therefore, we attribute this pressure-induced asymmetric Bragg peak broadening above 16 GPa to a structural transition.

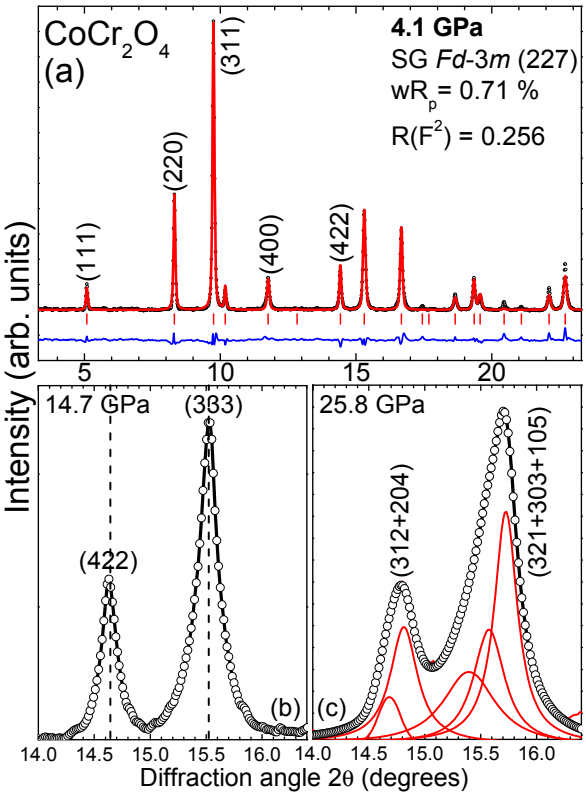

FIG. 2: (Color online) Example of (a) a Rietveld refinement for the *Fd*-3*m* phase at 4.1 GPa. Dots correspond to the measured spectrum, whereas the red and blue solid lines represent the best refinement and the difference between the experimental and refined pattern, respectively. Vertical ticks mark the Bragg peak positions. An expanded view of the (311) and (222) *Fd*-3*m* Bragg peaks before [(b) @ 14.7 GPa] and [(c) @ 25.8 GPa] after the cubic-tetragonal transition is also displayed.

The observed high-pressure phase could be assigned to a tetragonal distortion of the original cubic structure. Due to the broadening of the Bragg peaks after the cubic-tetragonal transition, which arises partly from the aforementioned peak splittings, only the lattice parameters could be extracted for the high-pressure phase. For the same reason, we could not assign a unique space group for the high-pressure phase; nevertheless, and by taking into account the structural behavior of similar Cr-based spinels under pressure[11,12], we have employed the tetragonal SG $I4_1/amd$ (Z=4) for our refinements. The high-pressure $I4_1/amd$ phase can be easily derived from the starting *Fd*-3*m* structure: the *c*-axis in the two structures is common, whereas the a_{tetr}-axis equals the cubic lattice parameter a_{cub} divided by $\sqrt{2}$.

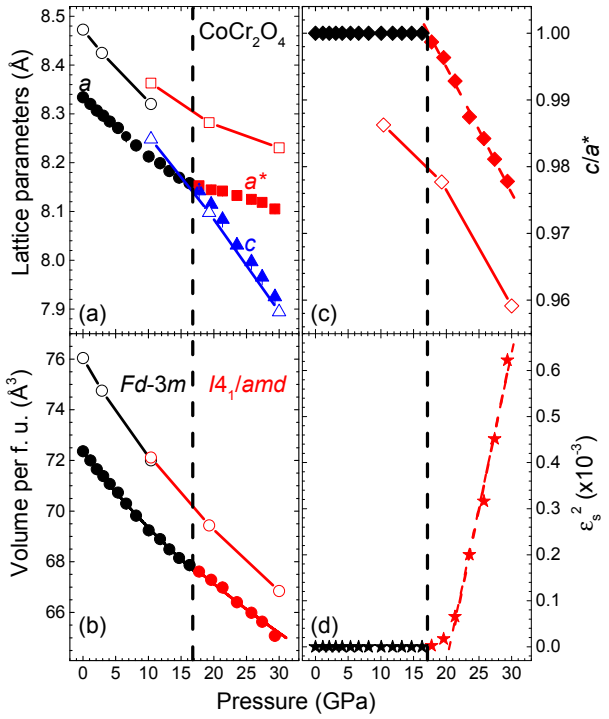

FIG. 3: (Color online) The evolution of (a) the lattice parameters, (b) the unit cell volume per formula unit, and the (c) axial ratio as a function of pressure for both the *Fd*-3*m* and tetragonal phases of $CoCr_2O_4$. The vertical dashed lines mark the onset of the (experimental) structural transition, whereas the open symbols represent the calculated structural parameters with DFT (black for the *Fd*-3*m* paramagnetic and red for the $I4_1/amd$ ferrimagetic phase, respectively). Notice that we employ the pesudocubic $a^*(=a_{tet}\sqrt{2})$ lattice constant for direct comparison. (d) Plot of the square of the symmetry-breaking tetragonal strain $\varepsilon_S^2 \approx [(c-a^*)/a_{cub}]^2$ against pressure, where a^* and c are the lattice parameters of the tetragonal phase, and a_{cub} is the lattice parameter of the cubic phase extrapolated into the stability field of the tetragonal phase. The dashed red line represents the linear fit expected from Landau theory.

The obtained lattice parameters for both phases are plotted in **Fig. 3(a)**. We employ the pseudocubic $a^*=a_{tetr}\sqrt{2}$ tetragonal lattice constant for direct comparison. The a^*-axis does not show any visible change at the transition point, whereas the c-axis contracts by ~0.13% with respect to the *Fd*-3*m* lattice parameter [**Fig. 3(a)**]. From the experimental P-V data alone, however, it is difficult to determine whether there is any volume discontinuity at the transition point [**Fig. 3(b)**]. Since the cubic-tetragonal transition in $CoCr_2O_4$ is expected to be of second-order from space group symmetry considerations[59], the Landau theory of phase transitions can be used for verification[60,61]. For this reason, we plot the square of the tetragonal strain ε_S against pressure in **Fig. 3(d)**; since the relationship between these two parameters is not linear, we classify the cubic-tetragonal transition as a *first-order structural transition*.

Further compression of the high-pressure tetragonal phase leads to the continuous decrease for both the a^*- and c-axes, with the c-axis being more compressible throughout the investigated pressure range [**Fig. 3(a)**]. This variation in the axial

pressure dependence is clearly captured via the continuous decrease of the tetragonal *c*/*a** axial ratio up to 30 GPa [**Fig. 3(b)**].

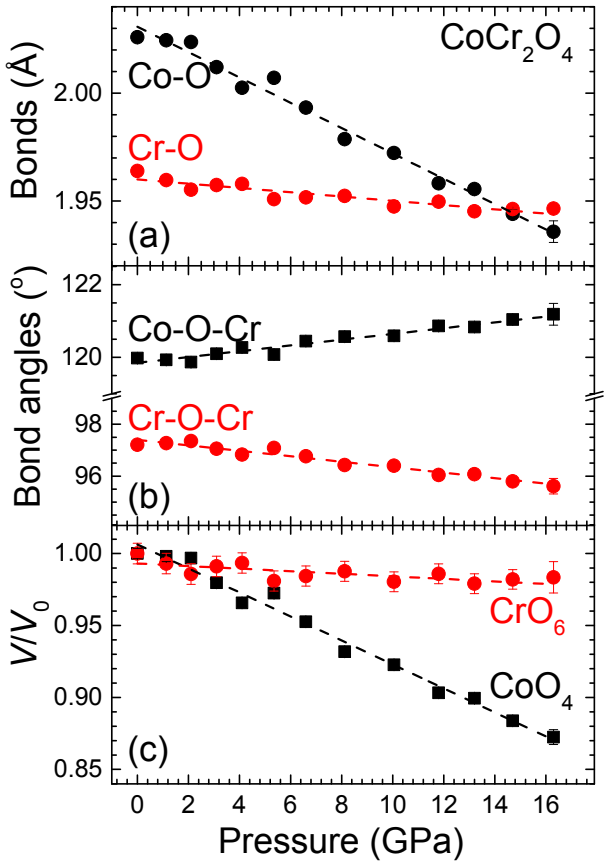

FIG. 4: (Color online) Pressure-induced variation of (a) the Co-O and Cr-O bond lengths, and (b) the Cr-O-Cr and Co-O-Cr bond angles for the *Fd*-3*m* phase of $CoCr_2O_4$. The error bars lie within the symbols. (c) The normalized polyhedral volume is also plotted as a function of pressure.

Regarding the *P*-*V* data of the cubic and tetragonal phases, we have fitted each phase with a separate B-M EOS function[30] [**Fig. 3(c)**]. The derived elastic parameters are: V_0/Z=72.4 Å^3 (as measured), B_0=209(±8) GPa, and B'_0=5(±1) for the cubic phase, and V_{Tr}/Z=67.6 Å^3 (as measured), B_{Tr}=313(±8) GPa, and B'_{Tr}=4(fixed) for the tetragonal phase at the transition pressure point P_{Tr}=17.8 GPa. The bulk modulus B_0 of the cubic $CoCr_2O_4$ phase is consistent with the bulk moduli reported for other Cr-based oxospinels[54].

Turning finally to the interatomic parameter evolution against pressure for the *Fd*-3*m* phase, we display the two different metal-oxygen bond lengths and the interatomic bond angles as a function of pressure in **Figs. 4(a, b)**. The longer Co-O bond distance decreases much faster compared to the Cr-O bond, which is almost incompressible [**Fig. 4(a)**]. This is also evidenced by the significant pressure-induced relative volume change of the two different CoO_4 and CrO_6 polyhedral units comprising the spinel structure [**Fig. 4(c)**]. The two bond lengths become equivalent near 15 GPa, just

before the tetragonal distortion. On the contrary, the two intercationic Co-O-Cr and Cr-O-Cr bond angles are almost pressure insensitive [**Fig. 4(b)**]. This bond angle resilience against pressure appears to be a common feature among Cr-based spinels[11,12].

B. High-pressure Raman investigation

In order to probe the lattice dynamics of $CoCr_2O_4$, we have employed high-pressure Raman spectroscopy. The results are displayed in **Fig. 5**. For the starting *Fd*-3*m* phase, we can detect all five of the expected Raman-active modes[62,63] (**Table I**). The *Fd*-3*m* Raman modes exhibit normal behavior upon pressure increase, i.e. their frequencies increase under compression [**Fig. 5(b)** & **Table I**]. The effect is more pronounced for the $F_{2g}(2)$, $F_{2g}(3)$, and A_{1g} modes assigned to stretching vibrations[63], since the respective bond lengths are more compressible than the bond angles [**Fig. 4(a, b)**].

Except from the Raman-active modes of the *Fd*-3*m* phase, a low-intensity band (termed M) located at ~580 cm^{-1} could be resolved near 5 GPa (**Fig. 5** & **Table I**). Careful inspection of the Raman spectra indicates that this band resides at the base of the much more intense $F_{2g}(2)$ mode at ambient conditions, and is gradually separated upon compression. Given its "unexpected" presence and extremely low relative intensity compared to the spinel Raman-active bands, we attribute this M mode to a local defect/impurity of crystalline $CoCr_2O_4$. Actually, both the extrapolated ambient-pressure frequency and the pressure dependence of the M band coincide with the A_{1g} mode of Cr_2O_3[64] (**Table I**). Hence, our assignment for this extra M mode as a local defect/impurity band appears reasonable.

As for the high-pressure tetragonal $I4_1/amd$ phase, ten Raman-active modes are expected[65]. In our case, however, we could not observe either any new Raman-active modes (something which excludes the pressure-induced cationic inversion scenario as already discussed[58]), or subtle/abrupt frequency shifts of the measured Raman modes in the vicinity of the transition point [**Fig. 5(b)** & **Table I**]. Even though the clear distinction between the *Fd*-3*m* and $I4_1/amd$ phases is not always possible from Raman spectroscopy (e.g. the tetragonally-distorted $NiCr_2O_4$ spinel does not show the Raman features expected for the $I4_1/amd$ phase[66]), a more thorough analysis of the measured Raman bands reveals delicate changes near the cubic-tetragonal transition.

In particular, the widths of the $F_{2g}(1)$ and E_g modes tend to increase beyond ~17 GPa [**Fig. 5(c)**]. Since (a) we have employed He as PTM and (b) we do not observe similar behavior (broadening) in the widths of the remaining Raman modes [the width of the A_{1g} mode exhibits an almost linear decrease under pressure, **Fig. 5(c)**], we can safely exclude any extrinsic effects such as non-hydrostaticity as the reason behind these width modifications. On the contrary, we assign these pressure-induced peak broadenings to the tendency of the respective Raman modes to split above that pressure. Given that the tetragonal distortion of the cubic structure is small (**Fig. 3**), the detection of these Raman peak splittings is probably hindered by the resolution of the spectrometer (~2 cm^{-1}). Hence, the pressure-induced peak broadenings for specific

Raman-active modes can serve as an indirect probe for the structural distortion of the spinel phase above 17 GPa, in excellent agreement with our XRD study.

We should finally mention that the integrated intensities of the E_g and $F_{2g}(3)$ modes exhibit substantial increase after the cubic-tetragonal transition[54]. This Raman intensity enhancement can most likely be attributed to resonance effects coming into play after the structural distortion, since (a) both the Co^{2+} and Cr^{3+} intra *d-d* electronic excitations lie just below the incident laser energy (E_{laser}=2.3 eV) at ambient conditions[22], and (b) both of these *d-d* transitions are expected to shift towards higher energies upon compression[14], thus sastisfying resonance Raman conditions beyond a certain pressure.

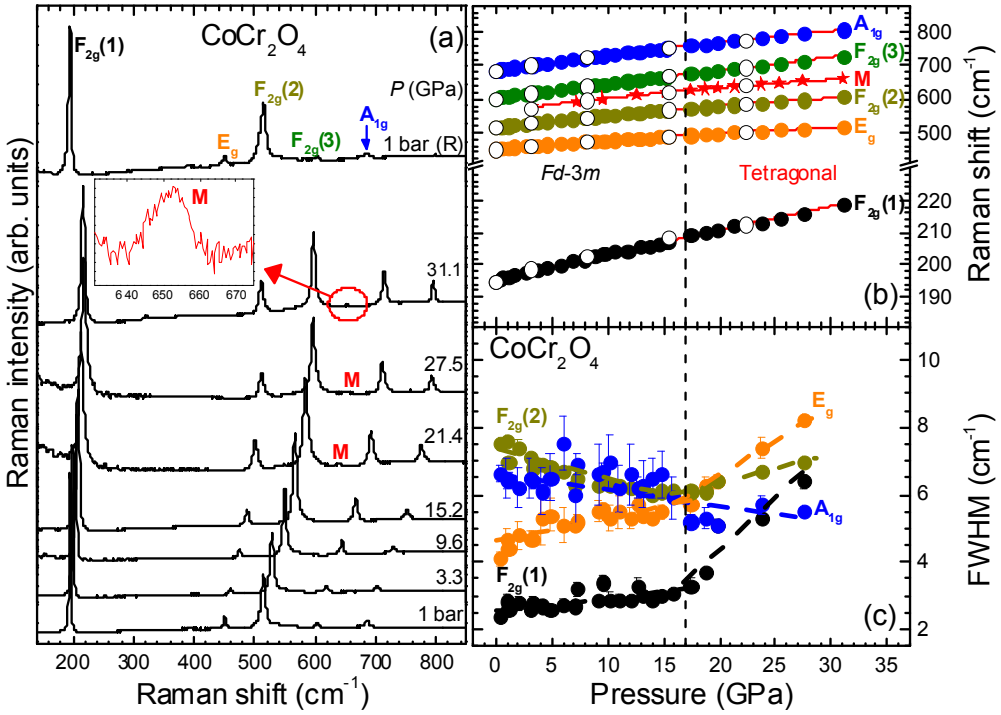

FIG. 5: (Color online) (a) Selected Raman spectra of $CoCr_2O_4$ at various pressures (λ=532 nm, T=300 K). The assignment of each mode is provided. (b) Raman mode frequencies and (c) selected full widths at half maximum (FWHM) as a function of pressure. Closed and open circles depict measurements upon increasing and decreasing pressure.

Table I: Assignment[62,63], frequencies, pressure coefficients, and the mode Gruneisen parameters γ of the Raman modes of $CoCr_2O_4$. The pressure depencence of the Raman-active modes is described by the relation: $\omega(P)=\omega_0+\alpha P+bP^2$, where frequeny ω_0 is in cm^{-1} and pressure P in GPa. The Gruneisen parameters γ are determined from the relation: $\gamma=(B_0/\omega_0)x(\partial\omega/\partial P)$, where B_0=209 GPa (this work).

Mode	ω_{Tr} (cm^{-1})	$\partial\omega/\partial P$ (cm^{-1}/GPa)	$\partial^2\omega/\partial P^2$ (cm^{-1}/GPa^2)	γ
$F_{2g}(1)$	195.7(1)	0.75	-	0.8
E_g	452.2(2)	2.6	-0.02	1.2
$F_{2g}(2)$	516.2(3)	3.8	-0.03	1.54
$F_{2g}(3)$	605.8(3)	4	-	1.38
A_{1g}	687.6(3)	4.6	-0.03	1.4
M	563.2(9)	4.3(1)	-0.04	-

C. Calculated magnetic properties

We have additionally conducted *ab initio* calculations for understanding the effect of pressure on the magnetic properties of $CoCr_2O_4$ under pressure. Comparison between the experimental and calculated structural parameters[54] shows that the lattice parameter *a* for both the cubic and tetragonal phases of $CoCr_2O_4$ are overestimated [**Fig. 3(a)**]. Nevertheless, the trends between the calculated and experimental structural parameters under pressure are in very good agreement [**Fig. 3(a)-(c)**].

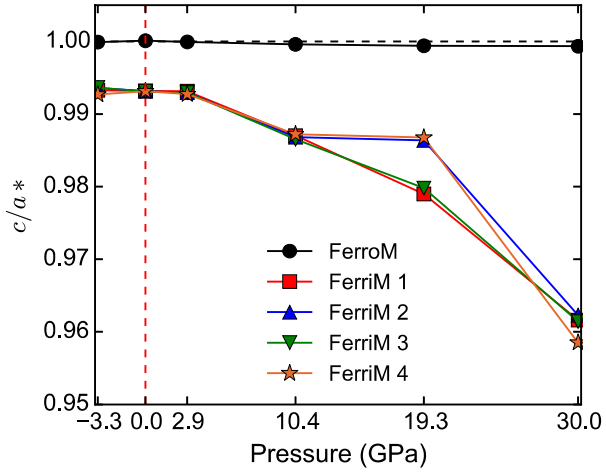

FIG. 6: (Color online) The axial ratio *c*/*a** as a function of pressure for different magnetic configurations of $CoCr_2O_4$. FerroM stands for the ferromagnetic case, whereas FerriM stand for the ferrimagnetic cases with four equivalent ways to alter the Cr^{3+} and Co^{2+} spin-ups and spin-downs (see text).

In **Fig. 6** we plot the axial ratio *c*/*a** dependence against pressure assuming different magnetic configurations for $CoCr_2O_4$. The FerroM phase (black circles) stands for all Cr^{3+} and Co^{2+} spin-up (or all spin-down). The FerriM phases (colored symbols) stand for half Cr^{3+} spin-up in the same plane on the *c*-axis and the other half

Cr^{3+} spin-down, with all Co^{2+} spin-up (or all spin-down). The energy surface shows a single minimum point when manually varying the c/a^* axial ratio at a high pressure value[54], confirming the results from the relaxation. It is clear that the ferrimagnetic state *always* favors a $c/a^*<1$, i.e. a tetragonal structure; application of external pressure leads to the enhancement of the tetragonal distortion. Interestingly, a tetragonal deviation from the cubic symmetry is suspected for $CoCr_2O_4$ upon entering the ferrimagnetic state below ~96 K, even though such transition has not been observed directly[21].

Furthermore, we have also checked the possibility of an orthorhombic distortion instead of a tetragonal one for the ferrimagnetic state, another possible structural modification observed in Cr-spinels upon magnetic ordering[67]. In order to achieve this, we relaxed the ferrimagnetic cell assuming an orthorhombic initial structure with slightly different *a*, *b*, and *c* values and let them freely relax for each given volume. The resulting *a*/*b* ratio values deviate below 0.4 % from 1 within the simulation range, i.e. from -3.3 GPa to 30 GPa. Since the calculated *a*/*b* values are very close to 1 (c/a^* is nearly the same as in the tetragonal cell), we conclude that the ferrimagnetic configuration is accompanied by a tetragonal distortion.

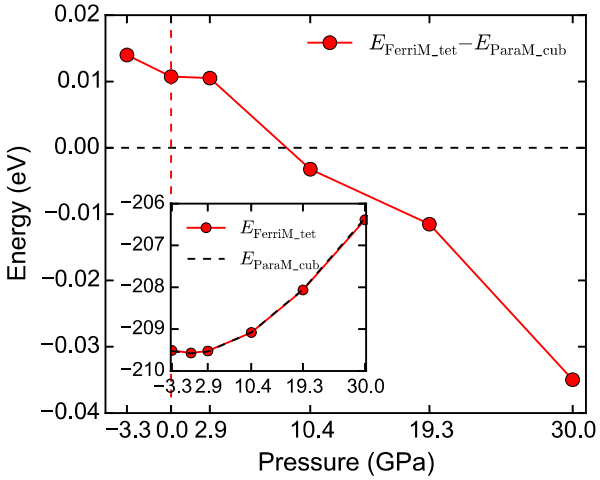

FIG. 7: (Color online) Energy difference between the paramagnetic cubic (ParaM_cub) and the ferrimagnetic tetragonal (FerriM_tet) phases of $CoCr_2O_4$ as a function of pressure.

In **Fig. 7** we display the energy difference between the paramagnetic cubic and the ferrimagnetic tetragonal phases of $CoCr_2O_4$ as a function of pressure. We can notice a crossing between the two phases close to 10 GPa, indicating that higher pressure favors the ferrimagnetic tetragonal ground state. In order to gain further insight on the magnetic properties, we have extracted the values of the magnetic exchange interactions J_{AA}, J_{BB}, and J_{AB} assuming a cubic structure at different pressures (**Table II**), and by employing the Heisenberg model of Ref. 68. The calculated J_{AA}, J_{AB}, and J_{BB} values at 0 GPa ($U_{A\ (Co)}$ = 3.3 eV, $U_{B\ (Cr)}$ = 3.7 eV) are in very good agreement with previous results obtained from LSDA+U[68]. Compression leads to the strengthening of all *J* interactions, a direct result from the shrinkage of the lattice. According to the theory developed by Lyons, Kaplan, Dwight, and Menyuk[69](LKDM), the magnetic ground state and/or the magnetic frustration of a

spinel compound can be described by the parameter $u \approx J_{BB}/J_{AB}$. In particular, the larger the magnitude of u, the more frustrated the respective spinel. Given that the J_{BB} coupling constant displays a larger enhancement under pressure compared to J_{AB} (**Table II**), we can reasonably anticipate the enhancement of the magnetic frustration in $CoCr_2O_4$ under compression. Such hypothesis is consistent with experimental high-pressure magnetization studies[23–25].

Table II: Calculated magnetic exchange interactions assuming a cubic structure for all four constructed magnetic configurations at various pressures by employing the Heisenberg model of Ref. 68 (here: $U_{A\ (Co)}$ =3.3 eV, $U_{B\ (Cr)}$ = 3.7 eV). The term A stands for the "base" energy without the addition of magnetic contribution.

P (GPa)	V (Å^3)	A (eV)	J_{AA} (meV)	J_{AB} (meV)	J_{BB} (meV)
-3.3	310.00	-209.497	-0.84	-8.11	-2.10
0	304.00	-209.555	-0.92	-9.00	-2.97
2.9	299.00	-209.500	-1.00	-9.83	-3.37
10.4	288.00	-209.041	-1.20	-11.95	-4.86
19.3	277.00	-208.003	-1.47	-14.58	-6.71
30	266.00	-206.292	-1.82	-17.86	-8.93

In order to look for any electronic effects taking place near the magneto-structural transition, we have calculated the spin-resolved total density of states (TDOS) for the two magnetic/structural configurations of $CoCr_2O_4$ at three different pressures: 0 GPa, 10 GPa (close to the calculated transition point), and 30 GPa (**Fig. 8**). Application of external pressure induces the broadening of the electronic bands for both phases due to lattice shrinkage, which in turn leads to slightly smaller band gap values. In particular, the band gap of the paramagnetic cubic phase decreases from 2.77 eV to 2.64 eV. On the other hand, the band gap of the spin-up states for the ferrimagnetic tetragonal phase does not change under pressure (the 0 GPa value is 2.87 eV), whereas the band gap of the spin-down states drops from 2.55 eV to 2.40 eV. In addition, the Bader charge analysis for both the cubic and tetragonal phases does not show considerable changes throughout the examined pressure range[54]. Overall, the general shape of the TDOS and Bader charge transfer do not change much upon compression, indicating that the pressure-induced cubic-tetragonal transition is not accompanied and/or induced by electronic charge effects.

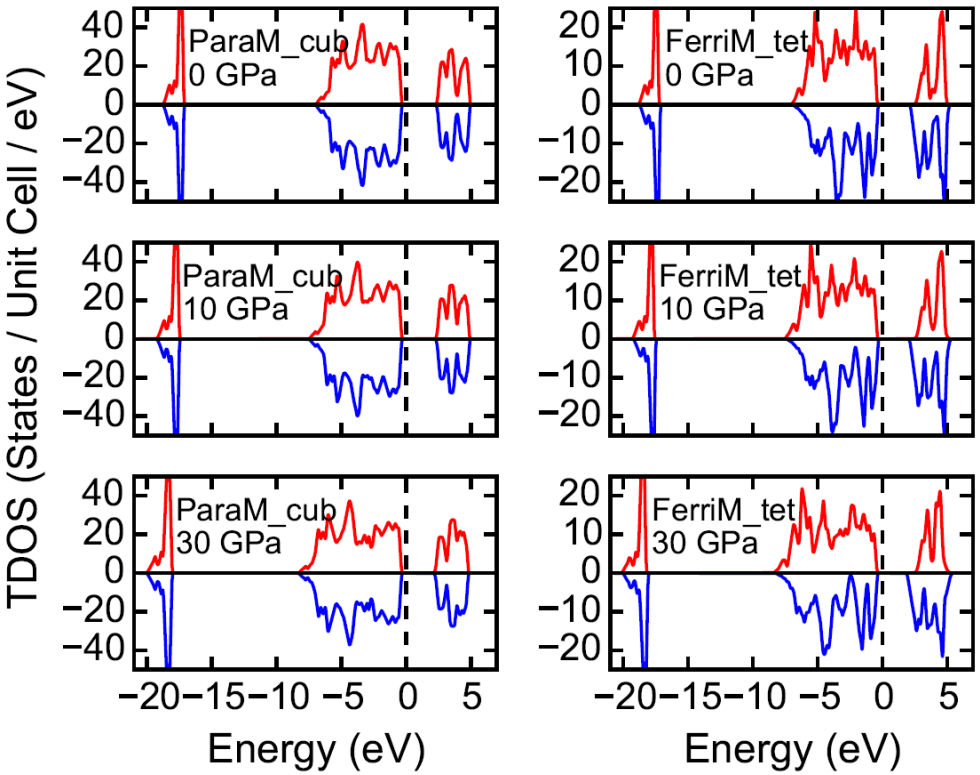

FIG. 8: (Color online) Spin-resolved total density of states (TDOS) of the paramagnetic cubic (ParaM_cub) and the ferrimagnetic tetragonal (FerriM_tet) phases at various pressures. The red and blue lines correspond to spin-up and spin-down states, respectively. Notice that for the ParaM_cub phase, the spin-up and spin-down states are identical.

D. Discussion

Systematic high-pressure structural investigations on oxide spinels have demonstrated that the starting cubic *Fd*-3*m* phase transforms into the denser $CaFe_2O_4$-, $CaTi_2O_4$-, or a $CaMn_2O_4$-type structures upon sufficient compression[70,71]. Similar high-pressure studies on Cr-based oxospinels, however, appear to deviate somewhat from this established trend. In particular, a theoretical study proposed the decomposition of the $MgCr_2O_4$, $MnCr_2O_4$, and $ZnCr_2O_4$ spinels into their constituent oxides under pressure[72]. Subsequent experimental studies, however, on $ZnCr_2O_4$[73] and $MgCr_2O_4$[74] did not verify the decomposition scenario. In particular, $ZnCr_2O_4$ undergores a cubic-orthorhombic transition beyond 30 GPa[73], whereas $MgCr_2O_4$ adopts a tetragonal $I4_1/amd$ structure above 20 GPa (c/a*=0.8 at the transition point)[74]; high-pressure structural data have not been reported for $MnCr_2O_4$ up to now. On the other hand, pressure-induced decomposition was claimed to take place for the tetragonally-distorted $NiCr_2O_4$ spinel from Raman studies[66]. Furthermore, the $FeCr_2O_4$ spinel transforms also into the $I4_1/amd$ structure at 12 GPa (c/a*≈1 at the transition point)[75]. Finally, $CdCr_2O_4$ adopts an orthorhombic $CaFe_2O_4$-type phase after combined high-pressure and high-temperature treatment[76]; a recent high-pressure infrared investigation indicated that a phase transition takes place above 15 GPa at

room temperature as well[14]. Hence, the observed cubic-tetragonal distortion observed for $CoCr_2O_4$ above 16 GPa complies with the structural trend of Cr-based oxospinels under pressure.

Turning now to the possible driving force behind the observed pressure-induced structural distortion, these consist of underlying electronic (orbital and/or charge)[14,59,75,77] and/or magnetic[22,78] effects. Regarding the electronic part, we have already mentioned that our TDOS and Bader charge transfer calculations did not reveal any significant changes in the vicinity of the cubic-tetragonal transition. As for a possible pressure-induced orbital, i.e. Jahn-Teller effect in $CoCr_2O_4$ as in isostructural $FeCr_2O_4$[75], we remind here that both Co^{2+} ($3d^7$: e^4 t_2^3) and Cr^{3+} ($3d^3$: t_{2g}^3 e_g^0) cations are orbitally-inactive in the starting *Fd*-3*m* phase (**Fig. 1**). As a result, a plausible Jahn-Teller effect in this system would require/induce appreciable intercationic charge transfer in the vicinity of the cubic-tetragonal transition point, something which is also excluded by our Bader charge transfer calculations[54]. Therefore, we conclude that the magnetic component is the key ingredient behind the cubic-tetragonal transition in $CoCr_2O_4$.

By taking into account similar magnetoelastic transitions in Cr-based spinels[6,7,22], we *speculate* that the cubic-tetragonal transition is triggered by the enhancement of the magnetic frustration in $CoCr_2O_4$, resulting from the "disproportionate" strengthening of the various magnetic exchange interactions J_{AA}, J_{BB}, and J_{AB} under pressure (**Table II**). This magnetic frustration is partially relieved by the lowering of the crystalline symmetry from cubic to tetragonal. Finally, and given that ferroelectricity for $CoCr_2O_4$ requires the magnetically frustrated state[3,18–21], we estimate that pressure will probably *enhance* the macroscopic electrical polarization. More appropriate experimental probes will be needed, however, in order to verify our assumptions.

IV. CONCLUSIONS

In summary, we have explored the structural, vibrational, magnetic, and electronic behavior of the multiferroic $CoCr_2O_4$ spinel up to 30 GPa by a combination of experimental and *ab initio* methods. Our investigations reveal a reversible tetragonal distortion of the starting cubic structure above 16 GPa. Our DFT studies indicate that this structural modification is not accompanied by any appreciable electronic effects. On the other hand, our calculations indicate that the main driving force behind the observed structural transition in $CoCr_2O_4$ is of magnetic origin, probably due to the disproportionate strengthening of the various magnetic exchange interactions.

ACKNOWLEDGEMENTS

Portions of this work were performed at HPCAT (Sector 16), Advanced Photon Source (APS), Argonne National Laboratory. HPCAT operations are supported by DOE-NNSA under Award No. DE-NA0001974 and DOE-BES under Award No. DE-FG02-99ER45775, with partial instrumentation funding by NSF. The Advanced

Photon Source is a U.S. Department of Energy (DOE) Office of Science User Facility operated for the DOE Office of Science by Argonne National Laboratory under Contract No. DE-AC02-06CH11357. We would like to thank Dr. G. Shen for kindly offering us the necessary beamtime for the experiment.

We would also like to thank Dr. S. Tkachev at GeoSoilEnviroCARS (Sector 13), APS-ANL for his assistance with the DAC gas loading. Use of the COMPRES-GSECARS gas loading system was supported by COMPRES under NSF Cooperative Agreement EAR 11-57758 and by GSECARS through NSF grant EAR-1128799 and DOE grant DE-FG02-94ER14466. This research used resources of the Advanced Photon Source, a U.S. Department of Energy (DOE) Office of Science User Facility operated for the DOE Office of Science by Argonne National Laboratory under Contract No. DE-AC02-06CH11357. We would like to thank support from NSF grant No. CMMI 1234777. We acknowledge use of computational resources from the Tandy Supercomputing Center and the Ohio Supercomputing Center.

This research has been partially supported by the DFG via TRR 80 (Augsburg-Munich).

*Corresponding authors: iliefthi@gmail.com and ywang235@oakland.edu

[1] J. Hemberger, P. Lunkenheimer, R. Fichtl, H. A. Krug von Nidda, V. Tsurkan, and A. Loidl, Nature **434**, 364 (2005).

[2] S. Weber, P. Lunkenheimer, R. Fichtl, J. Hemberger, V. Tsurkan, and A. Loidl, Phys. Rev. Lett. **96**, 157202 (2006).

[3] Y. Yamasaki, S. Miyasaka, Y. Kaneko, J.-P. He, T. Arima, and Y. Tokura, Phys. Rev. Lett. **96**, 207204 (2006).

[4] K. Dey, S. Majumdar, and S. Giri, Phys. Rev. B **90**, 184424 (2014).

[5] H. W. Lehmann and G. Harbeke, Phys. Rev. B **1**, 319 (1970).

[6] F. Yokaichiya, A. Krimmel, V. Tsurkan, I. Margiolaki, P. Thompson, H. N. Bordallo, A. Buchsteiner, N. Stusser, D. N. Argyriou, and A. Loidl, Phys. Rev. B **79**, 064423 (2009).

[7] S. Bordacs, D. Varjas, I. Kezsmarki, G. Mihaly, L. Baldassarre, A. Abouelsayed, C. A. Kuntscher, K. Ohgushi, and Y. Tokura, Phys. Rev. Lett. **103**, 077205 (2009).

[8] T. Rudolf, C. Kant, F. Mayr, J. Hemberger, V. Tsurkan, and A. Loidl, New J. Phys. **9**, 76 (2007).

[9] V. Gnezdilov, P. Lemmens, Y. G. Pashkevich, C. Payen, K. Y. Choi, J. Hemberger, A. Loidl, and V. Tsurkan, Phys. Rev. B **84**, 045106 (2011).

[10] G. N. P. Oliveira, A. M. Pereira, A. M. L. Lopes, J. S. Amaral, A. M. dos Santos, Y. Ren, T. M. Mendonca, C. T. Sousa, V. S. Amaral, J. G. Correia, and J. P. Araujo, Phys. Rev. B **86**, 224418 (2012).

[11] I. Efthimiopoulos, A. Yaresko, V. Tsurkan, J. Deisenhofer, A. Loidl, C. Park, and Y. Wang, Appl. Phys. Lett. **103**, 201908 (2013).

[12] I. Efthimiopoulos, A. Yaresko, V. Tsurkan, J. Deisenhofer, A. Loidl, C. Park, and Y. Wang, Appl. Phys. Lett. **104**, 11911 (2014).

[13] Y. Amiel, G. K. Rozenberg, N. Nissim, A. Milner, M. P. Pasternak, M. Hanfland, and R. D. Taylor, Phys. Rev. B **84**, 224114 (2011).

[14] K. Rabia, L. Baldassarre, J. Deisenhofer, V. Tsurkan, and C. A. Kuntscher, Phys. Rev. B **89**, 125107 (2014).

[15] H. Ueda and Y. Ueda, Phys. Rev. B **77**, 224411 (2008).

[16] V. Tsurkan, S. Zherlitsyn, S. Yasin, V. Felea, Y. Skourski, J. Deisenhofer, H. A. Krug von Nidda, J. Wosnitza, and A. Loidl, Phys. Rev. Lett. **110**, 115502 (2013).

[17] K. Tomiyasu, J. Fukunaga, and H. Suzuki, Phys. Rev. B **70**, 214434 (2004).

[18] Y. J. Choi, J. Okamoto, D. J. Huang, K. S. Chao, H. J. Lin, C. T. Chen, M. van Veenendaal, T. A. Kaplan, and S.-W. Cheong, Phys. Rev. Lett. **102**, 067601 (2009).

[19] G. Lawes, B. Melot, K. Page, C. Ederer, M. A. Hayward, T. Proffen, and R. Seshadri, Phys. Rev. B **74**, 024413 (2006).

[20] K. Singh, A. Maignan, C. Simon, and C. Martin, Appl.Phys. Lett. **99**, 172903 (2011).

[21] S. Yang, H. X. Bao, D. Z. Xue, C. Zhou, J. H. Gao, Y. Wang, J. Q. Wang, X. P. Song, Z. B. Sun, X.B. Ren, and K. Otsuka, J. Phys. D: Appl. Phys. **45**, 265001 (2012).

[22] V. Kocsis, S. Bordacs, D. Varjas, K. Penc, A. Abouelsayed, C. A. Kuntscher, K. Ohgushi, Y. Tokura, and I. Kezsmarki, Phys. Rev. B **87**, 064416 (2013).

[23] T. Kanomata, T. Tsuda, H. Yasui, and T. Kaneko, Phys. Let. A **134**, 196 (1988).

[24] S. Tamura, Phys. B **190**, 150 (1993).

[25] X. Chen, Z. Yang, Y. Xie, Z. Huang, L. Ling, S. Zhang, L. Pi, Y. Sun, and Y. Zhang, J. Appl. Phys. **113**, 17E129 (2013).

[26] H. K. Mao, J. Xu, and P. M. Bell, J. Geophys. Res. **91**, 4673 (1986).

[27] A. Hammersley, S. Svensson, M. Hanfland, A. Fitch, and D. Hausermann, High Press. Res. **14**, 235 (1996).

[28] B. H. Toby, J. Appl. Crystallogr. **34**, 210 (2001).

[29] R. B. von Dreele and A. C. Larson, Los Alamos Natl. Lab. Rep. No. LAUR 86-748 (1994).

[30] F. Birch, Phys. Rev. **71**, 809 (1947).

[31] G. Kresse and J. Furthmuller, Comput. Mater. Sci. **6**, 15 (1996).

[32] G. Kresse and J. Furthmuller, Phys. Rev. B **54**, 11169 (1996).

[33] G. Kresse and J. Hafner, Phys. Rev. B **49**, 14251 (1994).

[34] G. Kresse and J. Hafner, Phys. Rev. B **47**, 558 (1993).

[35] P. E. Blochl, Phys. Rev. B **50**, 17953 (1994).

[36] G. Kresse and D. Joubert, Phys. Rev. B **59**, 1758 (1999).

[37] J. P. Perdew, J. A. Chevary, S. H. Vosko, K. A. Jackson, M. R. Pederson, D. J. Singh, and C. Fiolhais, Phys. Rev. B **48**, 4978 (1993).

[38] J. P. Perdew, J. A. Chevary, S. H. Vosko, K. A. Jackson, M. R. Pederson, D. J. Singh, and C. Fiolhais, Phys. Rev. B **46**, 6671 (1992).

[39] L. Wang, T. Maxisch, and G. Ceder, Phys. Rev. B **73**, 195107 (2006).

[40] A. Jain, G. Hautier, S. P. Ong, C. J. Moore, C. C. Fischer, K. A. Persson, and G. Ceder, Phys. Rev. B **84**, 045115 (2011).

[41] A. Zunger, S. H. Wei, L. G. Ferreira, and J. E. Bernard, Phys. Rev. Lett. **65**, 353 (1990).

[42] A. van de Walle, P. Tiwary, M. de Jong, D. L. Olmsted, M. Asta, A. Dick, D. Shin, Y. Wang, L.-Q. Chen, and Z.-K. Liu, Calphad-Computer Coupling Phase Diagrams Thermochem. **42**, 13 (2013).

[43] A. van de Walle, M. Asta, and G. Ceder, Calphad-Computer Coupling Phase Diagrams Thermochem. **26**, 539 (2002).

[44] A. van de Walle, Calphad-Computer Coupling Phase Diagrams Thermochem. **33**, 266 (2009).

[45] R. F. W. Bader, *Atoms in Molecules: A Quantum Theory* (Oxford University Press, New York, 1990).

[46] F. W. Bieglerkonig, R. F. W. Bader, and T.-H. Tang, J. Comput. Chem. **3**, 317 (1982).

[47] F. W. Bieglerkonig, T. T. Nguyendang, Y. Tal, R. F. W. Bader, and A. J. Duke, J. Phys. B-At. Mol. Opt. Phys. **14**, 2739 (1981).

[48] G. Henkelman, A. Arnaldsson, and H. Jonsson, Comput. Mater. Sci. **36**, 354 (2006).

[49] E. Sanville, S. D. Kenny, R. Smith, and G. Henkelman, J. Comput. Chem. **28**, 899 (2007).

[50] Z. T. Y. Liu, D. Gall, and S. V. Khare, Phys. Rev. B **90**, 134102 (2014).

[51] Z. T. Y. Liu, X. Zhou, D. Gall, and S. V. Khare, Comput. Mater. Sci. **84**, 365 (2014).

[52] Z. T. Y. Liu, X. Zhou, S. V. Khare, and D. Gall, J. Phys. Cond. Mat. **26**, 25404 (2014).

[53] J. L. Roehl, Z. T. Y. Liu, and S. V. Khare, Mater. Res. Express **1**, 25904 (2014).

[54] See Supplemental Material at [] for the (a) XRD patterns of $CoCr_2O_4$ at various pressures, (b) experimental and calculated structural data for the cubic and tetragonal phases, (c) elastic parameters for various Cr-based spinels collected from the literature, (d) integrated intensities for the Raman-active modes, (e) construction parameters for the $CoCr_2O_4$ paramagnetic supercell, (f) ferrimagnetic energy surface against the axial ratio c/a^* at 26 GPa, and (g) the extracted ionic charge transfer from the Bader charge analysis of the paramagnetic cubic and ferrimagnetic tetragonal phases of CoCr2O4 at various pressures.

[55] L. Gerward, J. Z. Jiang, J. S. Olsen, J. M. Recio, and A. Waskowska, J. All. Comp. **401**, 11 (2005).

[56] J. Wittlinger, S. Werner, and H. Schulz, Acta Cryst. B **54**, 714 (1998).

[57] J. Wittlinger, S. Werner, and H. Schulz, Phys. Chem. Miner. **24**, 597 (1997).

[58] M. A. Laguna-Bercero, M. L. Sanjuan, and R. I. Merino, J. Phys. Cond. Mat. **19**, 186217 (2007).

[59] P. G. Radaelli, New J. Phys. **7**, 53 (2005).

[60] E. K. H. Salje, Phys. Reports **215**, 49 (1992).

[61] R. J. Hemley, J. Shua, M. A. Carpenter, J. Hua, H. K. Mao, and K. J. Kingma, Sol. St. Com. **114**, 527 (2000).

[62] M. Ptak, M. Maczka, A. Pikul, P. E. Tomaszewski, and J. Hanuza, J. Sol. St. Chem. **212**, 218 (2014).

[63] A. K. Kushwaha, Chin. J. Phys. **47**, 355 (2009).

[64] S.-H. Shim, T. S. Duffy, R. Jeanloz, C.-S. Yoo, and V. Iota, Phys. Rev. B **69**, 144107 (2004).

[65] C. M. Julien and M. Massot, J. Phys. Cond. Mat. **15**, 3151 (2003).

[66] Z. Wang, S. K. Saxena, P. Lazor, and H. S. C. O'Neill, J. Phys. Chem. Sol. **64**, 425 (2003).

[67] M. R. Suchomel, D. P. Shoemaker, L. Ribaud, M. C. Kemei, and R. Seshadri, Phys. Rev. B **86**, 054406 (2012).

[68] C. Ederer and M. Komelj, Phys. Rev. B **76**, 064409 (2007).

[69] D. H. Lyons, T. A. Kaplan, K. Dwight, and N. Menyuk, Phys. Rev. **126**, 540 (1962).

[70] Z. Wang, R. T. Downs, V. Pischedda, R. Shetty, S. K. Saxena, C. S. Zha, Y. S. Zhao, D. Schiferl, and A. Waskowska, Phys. Rev. B **68**, 094101 (2003).

[71] D. Errandonea, R. S. Kumar, F. J. Manjon, V. V. Ursaki, and E. V. Rusu, Phys. Rev. B **79**, 024103 (2009).

[72] M. Catti, F. F. Fava, C. Zicovich, and R. Dovesi, Phys. Chem. Miner. **26**, 389 (1999).

[73] D. Levy, V. Diella, A. Pavese, M. Dapiaggi, and A. Sani, Amer. Miner. **90**, 1157 (2005).

[74] W. Yong, S. Botis, S. R. Shieh, W. Shi, and A. C. Withers, Phys. Earth Planet. Inter. **196**, 75 (2012).

[75] A. Kyono, S. A. Gramsch, T. Yamanaka, D. Ikuta, M. Ahart, B. O. Mysen, H. K. Mao, and R. J. Hemley, Phys. Chem. Miner. **39**, 131 (2012).

[76] A. M. Arevalo-Lopez, A. J. Dos Santos-Garcia, E. Castillo-Martinez, A. Duran, and M. A. Alario-Franco, Inorg. Chem. **49**, 2827 (2010).

[77] L. Bai, M. Pravica, Y. Zhao, C. Park, Y. Meng, S. V. Sinogeikin, and G. Shen, J. Phys. Cond. Mat. **24**, 435401 (2012).

[78] J. Hemberger, T. Rudolf, H.-A. Krug von Nidda, F. Mayr, A. Pimenov, V. Tsurkan, and A. Loidl, Phys. Rev. Let. **97**, 087204 (2006).